Influence of isolated and clustered defects on electronic and dielectric properties of wüstite

Urszula D. Wdowik,[1] Przemysław Piekarz,[2] Paweł T. Jochym,[2] Krzysztof Parlinski,[2] and Andrzej M. Oleś[3,4]
[1]*Institute of Technology, Pedagogical University, Podchorążych 2, PL-30084 Kraków, Poland*
[2]*Institute of Nuclear Physics, Polish Academy of Sciences, Radzikowskiego 152, PL-31342 Kraków, Poland*
[3]*Marian Smoluchowski Institute of Physics, Jagiellonian University, Prof. S. Łojasiewicza 11, PL-30348 Kraków, Poland*
[4]*Max-Planck-Institut für Festkörperforschung, Heisenbergstrasse 1, D-70569 Stuttgart, Germany*
(Received 19 September 2014; revised manuscript received 19 December 2014; published 8 May 2015)

The influence of intrinsic Fe defects in FeO (either single cation vacancies or prototypical 4:1 vacancy clusters) on electronic and dielectric properties is studied within density-functional theory. The importance of local Coulomb interactions at Fe atoms is highlighted and shown to be responsible for the observed insulating Mott gap in FeO, which is reduced by the presence of defects. We investigate nonstoichiometric configurations of $Fe_{1-x}O$ with x ranging from 3% to 9%, and we find the aliovalent Fe cations in both the regular and interstitial lattice sites of the considered configurations. Furthermore, we show that the trivalent Fe ions, induced by both isolated and clustered Fe vacancies, introduce the empty band states inside the insulating gap, which decreases monotonically with increasing cation vacancy concentration. The $Fe_{1-x}O$ systems with high defect content become metallic for small values of the Coulomb interaction U, yielding an increase in the dielectric functions and optical reflectivity at low energies, in agreement with the experimental data. Due to the crystal defects, the infrared-active transverse optic phonons split and distribute over a wide range of frequencies, clarifying the origin of the exceptionally large spectral linewidths of the dielectric loss functions observed for wüstite in recent experiments.

DOI: 10.1103/PhysRevB.91.195111 PACS number(s): 63.20.−e, 63.20.D−, 61.05.F−, 77.80.B−

I. INTRODUCTION

Wüstite ($Fe_{1-x}O$) has challenged experimental and theoretical condensed matter physicists for over 60 years. In particular, the extent of its nonstoichiometry and its defect structure have been the subject of numerous experimental studies [1–5], and they are still a matter of discussion and a source of controversy [6]. Generally, these studies indicate that the crystal lattice of FeO is modified by the presence of Fe^{3+} cations and vacant Fe^{2+} sites. The crystal structure and charge distribution in $Fe_{1-x}O$ are very complex as the defects are likely to coalesce and arrange into clusters, which in turn can aggregate into larger defect structures. Although the size, shape, and distribution of the stable equilibrium defect clusters and their aggregates are still controversial, they are expected to vary with pressure, temperature, and composition [7]. Moreover, the clusters of defects are believed to order magnetically below the Néel temperature, $T_N = 198$ K.

Early theoretical investigations on nonstoichiometric FeO were mainly aimed at the mechanism of formation and stability of isolated Fe vacancies, prototypical 4:1-type clusters comprised of interstitial (tetrahedral) Fe^{3+} ion surrounded by four cation vacancies as well as complexes of such clusters [8–11]. The results of these studies indicate that wüstite favors the formation of 4:1-type clusters, which are major building blocks for further agglomeration and defect cluster growth [1]. Nevertheless, a substantial concentration of free vacancies can also be stabilized within the wüstite lattice.

Extended defect structures in $Fe_{1-x}O$ were rarely modeled using density-functional theory (DFT). Such simulations are still extremely demanding, as they require a proper description of the highly correlated nature of $3d$ electrons [12,13] and extensive ionic relaxations within large supercells to predict a correct ground state of $Fe_{1-x}O$. In our previous work, the DFT investigations have been performed for vacancy-defected FeO [14], uncovering pronounced changes of the electronic and vibrational properties induced by isolated cation vacancies. Recently, it was shown that polaronic distributions of charge resembling those in magnetite Fe_3O_4 emerge for the most stable defect structures in wüstite [15].

The point defects as well as their clusters are likely to affect the dielectric and optical properties of FeO. The results of various experiments [16–24] indicate some peculiar behavior of the measured optical quantities in wüstite and assign it to the native defects. However, a detailed explanation of the influence of such defects on the electronic and dielectric properties of FeO remains unclear. Furthermore, sensitivity of both the electronic structure and dielectric functions to the defect states as well as the extent of modifications induced by isolated or cluster defects still remains unexplored.

The present work extends the description of wüstite by investigating its electronic structure and dielectric properties as functions of the concentration of cation monovacancies and vacancy clusters. Our theoretical studies take into account strong local interactions of Coulomb type to properly describe the electronic properties and to better understand the mechanisms of the defect-induced changes in $Fe_{1-x}O$.

The paper is organized as follows. The details of the calculation method are described in Sec. II. Section III characterizes electronic properties, whereas Secs. IV A and IV B present a theoretical derivation of the dielectric properties and comparison with the experimental data, respectively. Finally, Sec. V summarizes the current results and provides conclusions.

II. METHODOLOGY

Calculations were performed within the spin-polarized DFT method using the VASP code [25]. Electron-ion interactions were described in the framework of the projector-augmented

wave (PAW) method [26]. Valence electrons of Fe and O atoms were represented by the $(3d^7 4s^1)$ and $(2s^2 2p^4)$ configurations, respectively. The gradient-corrected exchange-correlation functional in the form proposed by Perdew and Wang (GGA-PW91) [27] together with a plane-wave expansion up to 520 eV were applied. The effects of electron correlations beyond the generalized gradient approximation (GGA) were taken into account within the framework of GGA+U and the approach of Dudarev *et al.* [28], where a single parameter $U_{\text{eff}} = U - J$ determines an orbital-dependent correction to the DFT energy, with $J = 1$ eV denoting the local exchange interaction. Most of the present calculations were performed using $U_{\text{eff}} = 5$ eV, which is recognized as a realistic value while describing electron correlations between Fe($3d$) states [12–14]. Furthermore, it produces the lattice constant $a = 4.35$ Å , which remains in good agreement with various experimental studies [3,4]. Additional calculations with reduced values of U_{eff}, ranging from 2 to 4 eV, were carried out to investigate the influence of strong electron interactions and the screening processes due to defects on both the electronic structure and dielectric functions of wüstite.

A variety of experiments performed over decades indicates that FeO is always deficient in iron, and the concentration of vacancies in the oxygen sublattice is several orders of magnitude smaller than the concentration of iron vacancies [1,2]. Following the experimental evidence, we introduced vacancies into the cation sublattice of FeO and left its anion sublattice defect-free. The $Fe_{1-x}O$ structures with vacancy concentrations $x = 3\%$, 5%, 6%, and 9% were modeled by supercells [14,29,30]. Each initial supercell of $Fe_{1-x}O$ was derived from the basic 64-atom FeO supercell, which takes into consideration the antiferromagnetic (AFII) order [31] and comprises two ferromagnetic Fe sublattices differing in the orientation of the spin magnetic moments (spin-up and spin-down Fe sublattices). Neutral cation vacancies were created by removing the appropriate number of Fe atoms from the AFII supercell, whereas interstitial Fe atoms are inserted into the empty tetrahedral positions of such a supercell. The AFII supercell lacking one Fe atom corresponds to $Fe_{1-x}O$ with $x = 3\%$, while that with two Fe atoms absent conforms to $Fe_{1-x}O$ with $x = 6\%$. In the latter case, each of the ferromagnetic sublattices contains one Fe vacancy (V_{Fe}). There is, however, a number of possible configurations within the simulated supercell, with $x = 6\%$ differing among each other by $V_{\text{Fe}} - V_{\text{Fe}}$ distances. For further consideration, we have selected the configuration minimizing the system energy and corresponding to the $V_{\text{Fe}} - V_{\text{Fe}}$ distance of $1.22a$. The details of such calculations as well as a more comprehensive discussion are given in our previous work [14].

The $Fe_{1-x}O$ structures with $x \simeq 5\%$ and $x \simeq 9\%$ correspond to the 4:1-type clusters. The prototypical 4:1 cluster is schematically shown in Fig. 1. It is composed of an interstitial Fe atom surrounded by four cation vacancies arranged into a tetrahedron [8]. We note that due to the AFII magnetic ordering, three cation vacancies occupy the spin-up (or spin-down) ferromagnetic sublattice, while one cation vacancy is always located in the ferromagnetic sublattice with the reversed spin direction. The interstitial Fe ion may take on the spin direction of either a spin-up or spin-down cation sublattice. The AFII supercell containing one 4:1-type cluster

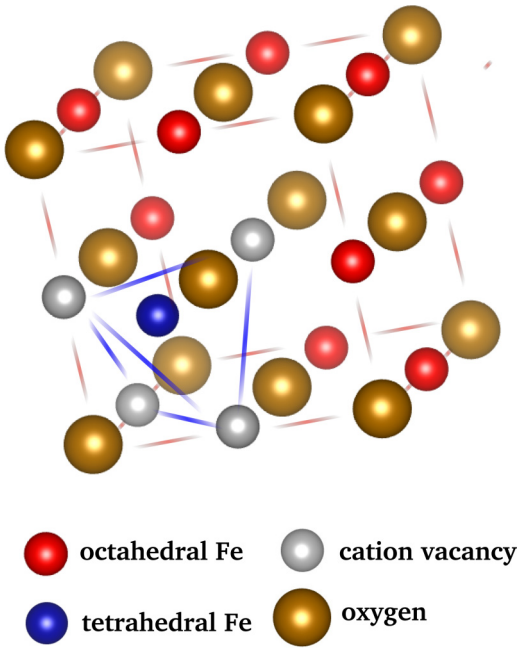

FIG. 1. (Color online) Schematic representation of the prototypical 4:1-type cluster with a single Fe ion in a tetrahedral configuration of $Fe_{1-x}O$.

corresponds to the overall cation deficiency of about 9%. Due to the cubic symmetry of the perfect FeO crystal, all possible locations of the 4:1-type cluster in the supercell are equivalent. The lower concentration of such defects, $x = 5\%$, is simulated by placing one 4:1 cluster into the supercell elongated in one of the main crystallographic axes. For convenience, we summarize the methodology of constructing isolated and clustered defects of wüstite in Table I.

Structural relaxations were performed for fixed volumes of the supercells followed from the optimized value of the defect-free FeO lattice. This approximation holds for the range of nonstoichiometries considered in the present work as the lattice constants of wüstite remain weakly dependent on x [3,4]. The atomic positions were relaxed without symmetry constraints imposed. Only in the case in which we determine the formation energies of defects were both volumes and atomic positions of the supercells relaxed. However, this procedure did not affect the final results, as the lattice parameters of the supercells containing defects changed by less than 1%. The Brillouin zones were sampled with the

TABLE I. The list of considered $Fe_{1-x}O$ configurations with the cation vacancy concentration (x), types of defects, sizes of supercells with respect to the crystallographic unit cell of defect-free FeO, total number of atoms in the supercell (N), and number of Fe atoms (N_{Fe}),

x (%)	Type of defect	Supercell size	N	N_{Fe}
0	stoichiometric	$2 \times 2 \times 2$	64	32
3	$1V_{\text{Fe}}$	$2 \times 2 \times 2$	63	31
5	4:1-type cluster	$4 \times 2 \times 2$	125	61
6	$2V_{\text{Fe}}$	$2 \times 2 \times 2$	62	30
9	4:1-type cluster	$2 \times 2 \times 2$	61	29

$\vec{k}$-point meshes of $2 \times 2 \times 2$ ($x = 3\%,6\%,9\%$) and $2 \times 2 \times 1$ ($x = 5\%$) generated according to the Monkhorst-Pack scheme. Convergence criteria for the residual forces and total energies of particular systems were set to 0.01 eV/Å and 0.1 meV, respectively. The complex dielectric functions as well as the intensities of the infrared-active phonon modes were obtained within the methodology proposed by Gajdoš *et al.* [32] and implemented in the VASP code.

The valence charges of Fe ions have been determined from the calculated electron contact densities at the Fe nuclei obtained within the full-potential (linearized) augmented plane wave plus local orbitals [FP-(L)APW + lo] method implemented in the WIEN code [33]. The wave functions have been expanded into spherical harmonics inside the nonoverlapping atomic spheres having the radii of a muffin-tin sphere R_{MT} and in the plane waves within the interstitial region. The R_{MT} belonged to the ranges of 1.93–2.03 a.u. for Fe and 1.66–1.74 a.u. for O atoms, with a value depending on the simulated system. The maximum l value for the expansion of the wave functions into the spherical harmonics inside the R_{MT} spheres was set to $l_{\max} = 10$, while for the expansion of the wave functions within the interstitial region, the plane-wave cutoff parameter $K_{\max} = 7/R_{\mathrm{MT}}^{\min}$ was applied. The charge density was Fourier-expanded up to $G_{\max} = 12\ \mathrm{Ry}^{1/2}$. Here, calculations were performed for the effective Coulomb interaction $U_{\mathrm{eff}} = 5$ eV, introduced in the rotationally invariant form proposed by Anisimov *et al.* [34]. Calculations have been carried out for the supercell volumes adopted from the pseudopotential method calculations. Only the atomic positions were relaxed within the FP-LAPW methodology with the force convergence of 0.01 mRy/a.u. and the symmetry constraints removed.

The valence states of Fe ions in $Fe_{1-x}O$ systems were identified according to the isomer shift (δ) systematics [35]. In general, the isomer shift is expressed as $\delta = \alpha(\rho - \rho_0)$, where ρ and ρ_0 stand for the electron contact densities at the resonant nucleus in a given matrix and reference material, respectively. The symbol α denotes the calibration constant characteristic for a particular nuclear transition. Our calculations are performed for the 14.41-keV transition in ^{57}Fe, and the isomer shifts are given with respect to metallic bcc α-Fe upon applying previously determined $\alpha = 0.291$ (a.u.)^3 mm/s [36]. More technical details of such calculations can be found in our earlier papers [30,36].

III. ELECTRONIC STRUCTURE

All considered $Fe_{1-x}O$ compositions reveal two different types of cation valence states, namely high-spin Fe^{2+} and high-spin Fe^{3+} residing both in the regular (R) and interstitial (I) positions of the cation sublattice. The compositions with 3% and 6% of isolated vacancies show both the Fe^{2+} and Fe^{3+} ions in R sites of the lattice, while those having 5% and 9% of vacancies and corresponding to the 4:1-type clusters exhibit Fe^{2+} and Fe^{3+} valence states in both the R and I lattice sites. Interstitial Fe becomes divalent when its spin is parallel to the spin direction of the magnetic sublattice from which three Fe atoms were removed, whereas it converts to the trivalent state if its spin is antiparallel to this sublattice (i.e., parallel to the ferromagnetic sublattice from which one Fe atom was removed). Thus, the interstitial Fe^{2+} has the opposite spin direction to the interstitial Fe^{3+}.

The total number of trivalent ions results from the number of cation vacancies created in the lattice since each vacancy is accompanied by two trivalent configurations. Therefore, six Fe^{3+} ions occupy R sites of the wüstite cation sublattice containing 4:1-type clusters, with Fe^{2+} ion at the I site, and five Fe^{3+} ions are located in the R lattice positions when the vacancy cluster involves interstitial Fe^{3+} ion. The compositions $x = 5\%$ and 9% with interstitial Fe^{3+} ions have lower energies than the respective compositions with interstitial Fe^{2+} ions by 14 and 8 meV/at, respectively. This indicates that the wüstite lattice favors interstitial Fe cations in the trivalent charge state, while the interstitial Fe^{2+} state can be considered as the metastable state. Nevertheless, it is interesting to note the essential differences between the electronic structures of these two configurations, which can be seen in Fig. 2.

First of all, the unoccupied electronic states due to Fe^{3+} ions appear in both the spin-up and spin-down channels for the system with the interstitial Fe^{3+} ion [Fig. 2(a)]. On the other hand, these states exist only in one channel direction in the system with the interstitially located Fe^{2+} ion [Fig. 2(b)]. In the latter case, the Fe^{3+} ions induced in the R lattice positions occupy solely a single magnetic sublattice, whereas they are

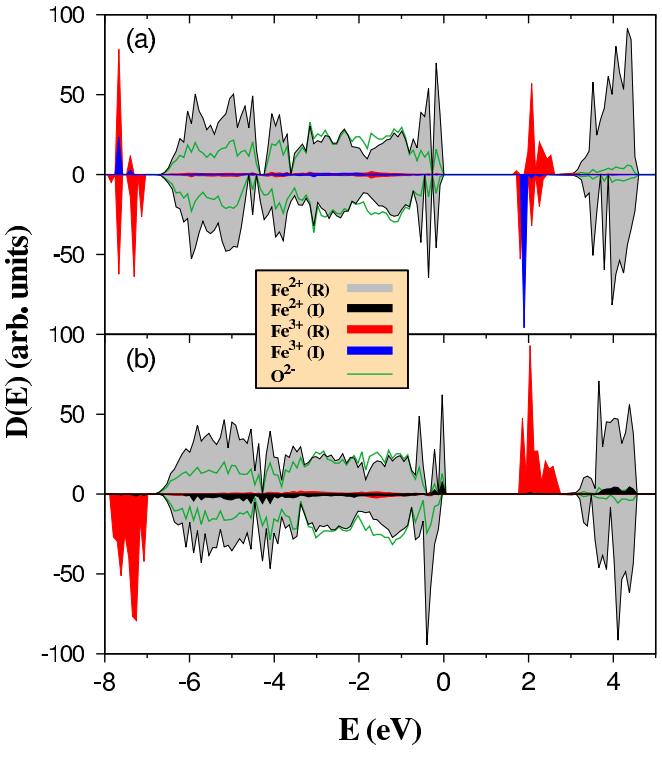

FIG. 2. (Color online) Densities of electron states calculated for $Fe_{1-x}O$ containing 4:1-type vacancy clusters ($x = 5\%$) at $U_{\mathrm{eff}} = 5$ eV. Configuration with (a) interstitial Fe^{3+} ion and (b) interstitial Fe^{2+} ion. Positive (negative) values represent the spin-up (spin-down) components. The $3d$ states of Fe^{2+} and Fe^{3+} ions residing in the regular (R) and interstitial (I) lattice sites are denoted by shaded areas (see the legend). The solid curve corresponds to O^{2-} states. The top of the valence band is taken as the reference energy (0 eV).

created in both magnetic sublattices in the former case. The interstitial Fe^{2+} ions introduce their electronic states into the same energy bands as the Fe^{2+} ions residing in the *R* lattice sites, as could be expected. Therefore, in the $Fe_{1-x}O$ systems containing either 4:1 vacancy clusters or free vacancies [14], the bottom of the conduction band as well as the states lying at about −8 to −7 eV below the top of the valence band consist of states formed by trivalent Fe cations. The empty states in the conduction band located above ∼3 eV from the top of the valence band arise from the divalent Fe cations occupying the *R* and *I* lattice sites. Each $Fe_{1-x}O$ configuration shows a significantly reduced insulating gap by the unoccupied electronic bands arising from the Fe^{3+} ions stabilized by cation vacancies.

The relative stability between monovacancies and vacancy clusters in $Fe_{1-x}O$ has been determined from the respective formation energies of neutral vacancies, defined as follows [37]:

$$E_{\text{form}} = E_d - E_{\text{FeO}} + nE_{\text{Fe}}, \tag{1}$$

where E_d is the total energy of the $Fe_{1-x}O$ supercell containing *n* vacancies, E_{FeO} is the total energy of the FeO supercell, and E_{Fe} denotes the energy of the Fe atom in the metallic Fe bcc crystal. It occurs that formation energies of systems with $x = 3\%$ and 6% are higher by 107 and 36 meV, respectively, per defect than the formation energy of systems containing a 4:1-type cluster ($x = 9\%$). Thus, the wüstite lattice seems to prefer the formation of vacancy clusters over the isolated cation vacancies. This result corresponds very well to the recent findings presented in Ref. [15].

In principle, the divalent and trivalent Fe cations residing in the *R* and *I* sites of the wüstite lattice are distinguishable by methods sensitive to changes in the electronic structure of a valence shell (e.g., Mössbauer spectroscopy), which are a consequence of changes in charge/spin states, electron localization/delocalization, and the defect structure. Indeed, the results of our calculations given in Table II indicate stronger screening of *s* electrons by 3*d* electrons for the high-spin Fe^{2+} ions compared to the high-spin Fe^{3+} ions, which results in higher and lower values of the corresponding isomer shifts, respectively. Moreover, the isomer shift of the interstitial Fe^{3+} is lower (0.384 mm/s) than the isomer shift of Fe^{3+} occupying the *R* sites (0.487 mm/s). Similar behavior is encountered for Fe^{2+} cations that exhibit slightly lower isomer shifts when located interstitially (1.039 mm/s) than octahedrally (1.108 mm/s). There is, however, no systematic dependence of $\delta(Fe^{2+})$ on the vacancy concentration *x* contrary to $\delta(Fe^{3+})$, which increases slightly with increased *x*.

TABLE II. Calculated ($x = 0\%,3\%,6\%,9\%$) and experimental (bold numbers) [4] isomer shifts of the Fe^{2+} and Fe^{3+} cations occupying the *R* and *I* sites of wüstite. Values of the isomer shifts for cations in the *R* positions are averaged over respective sites. Results are given for $U_{\text{eff}} = 5$ eV. According to the δ systematics [35], compounds containing high-spin Fe^{2+} show δ in the range of 1.0–1.5 mm/s, while for the compounds with high-spin Fe^{3+} the δ ranges from 0.3 to 0.6 mm/s.

x (%)	$\delta(Fe^{2+})$ (mm/s)	$\delta(Fe^{3+})$ (mm/s)
0	1.057 (*R*)	
2.9	**0.975–1.110**	**0.45**
3	1.103 (*R*)	0.445 (*R*)
4.8	**0.933–1.005**	**0.60**
6	1.097 (*R*)	0.453 (*R*)
9	1.108 (*R*), 1.039 (*I*)	0.476 (*R*), 0.382 (*I*)

The calculated isomer shift of the interstitial Fe^{3+} ion in $Fe_{1-x}O$ is close to that measured for stoichiometric $\alpha - Fe_2O_3$ (0.37–0.38 mm/s) [38] as well as that of the tetrahedral Fe^{3+} ion in stoichiometric Fe_3O_4 at 4.2 K (0.39 mm/s) [39]. Furthermore, the isomer shift of Fe^{3+} in the regular lattice sites of $Fe_{1-x}O$ is comparable to the experimental value of the octahedral Fe^{3+} ion in Fe_3O_4 (0.51 mm/s). There is also a correspondence between $\delta(Fe^{2+})$ in $Fe_{1-x}O$ and δ of octahedral Fe^{2+} in Fe_3O_4, since the Mössbauer resonance spectra of Fe_3O_4 obtained at 4.2 K reveal at least three components arising from the octahedral Fe^{2+} ions, for which the isomer shifts range from 0.81 to 1.02 mm/s [39]. The subspectra due to the octahedral Fe^{2+} ions result from the lowered symmetry of Fe_3O_4 below the Verwey transition temperature $T_V \approx 120$ K. We mention that the room-temperature Mössbauer spectra of Fe_3O_4 show the isomer shift for the octahedral cations of 0.66 mm/s resulting from the electron hopping between the octahedral Fe^{2+} and Fe^{3+} ions. It is advantageous to compare the calculated and measured isomer shifts of Fe cations in Fe-doped $Co_{1-x}O$, which is also a compound from the family of the simple 3*d* transition-metal monoxides, albeit showing a much lower degree of nonstoichiometry (1–3%) than wüstite. The high-spin Fe^{2+} and Fe^{3+} ions in $Co_{1-x}O$ give rise to the Mössbauer resonance lines having isomer shifts of 1.02 and 0.37 mm/s, respectively [30]. These values remain in a close relationship with those measured by the emission Mössbauer spectroscopy (1.12–1.14 mm/s for high-spin Fe^{2+} and 0.34–0.37 mm/s for high-spin Fe^{3+}) [40].

The Mössbauer spectra of realistic $Fe_{1-x}O$ samples [4,5] show much complexity as they are composed of several components reflecting quite a large number of different local environments accessible for Fe cations in the wüstite lattice. Although many attempts were undertaken [41], none of them described the local defect structure of wüstite in detail, as the hyperfine parameters of the Fe cations deduced from the empirical fits could only provide rough information on the statistically averaged environment of Fe^{2+} and Fe^{3+} in $Fe_{1-x}O$. Thus, the Mössbauer spectra of samples with the same stoichiometry could be successfully fitted using quite distinct phenomenological models. A difficulty in the interpretation of the experimental spectra presumably originates from a strong dependence of the wüstite defect structure on stoichiometry, and the population of certain defect arrangements in the $Fe_{1-x}O$ lattice may vary with composition in a complicated manner. Although the present theoretical research considers a limited number of possible defect configurations in wüstite, the results collected in Table II can be useful while interpreting the Mössbauer spectra of $Fe_{1-x}O$ because they provide a direct relationship between the local electronic structure of Fe cations (reflected by the respective isomer shifts), their location inside the wüstite lattice, and their immediate surrounding.

We have calculated the charges of ions using the Bader analysis (see Table III). Due to the hybridization effects,

TABLE III. The Bader charges and magnetic moments for different concentration of vacancies x. The values of magnetic moments obtained from the FP-LAPW method are given in parentheses. The Bader charges and magnetic moments are averaged over respective sites.

		Monovacancies		4:1 cluster	
x	0	3%	6%	5%	9%
		Bader charges (e)			
O^{2-}	7.32	7.28	7.25	7.28	7.26
$Fe^{2+}(R)$	6.68	6.70	6.71	6.69	6.69
$Fe^{2+}(I)$				6.62	6.57
$Fe^{3+}(R)$		6.40	6.38	6.33	6.33
$Fe^{3+}(I)$				6.30	6.31
		Magnetic moments (μ_B)			
$Fe^{2+}(R)$	3.74 (3.68)	3.67 (3.60)		3.69 (3.61)	
$Fe^{2+}(I)$				3.72 (3.64)	
$Fe^{3+}(R)$		4.19 (4.17)		4.20 (4.18)	
$Fe^{3+}(I)$				4.15 (4.12)	

the obtained charges differ from the ionic valences, and the difference between the Fe^{2+} and Fe^{3+} state is approximately $0.3e$. The trivalent cations exhibit enhanced spin magnetic moments comparing to those of divalent ones. We note that the magnetic moments remain dependent on U_{eff} but they depend weakly on x. Within U_{eff} ranging from 5 to 3 eV, they decrease linearly with decreasing U_{eff} by 0.085 μ_B/eV and 0.048 μ_B/eV for Fe^{3+} and Fe^{2+} cations, respectively. It is interesting to note that the magnetization isosurfaces around the Fe^{2+} and Fe^{3+} ions distinctly differ in their shapes, which can be seen in Fig. 3. The isosurface of Fe^{3+} is almost spherically symmetric, while that of Fe^{2+} contains cavities. The symmetric distribution of magnetization reflects nearly equal occupation of five $3d$ orbitals in the Fe^{3+} state, whereas one additional electron in the t_{2g} orbital of the Fe^{2+} ion destroys this symmetric population and contributes to the visible asymmetry in the magnetization isosurface.

It is worthwhile to analyze variation of the electronic properties of wüstite as a function of the Coulomb interaction parameter U_{eff}. Although the exact value of U_{eff} remains unknown, it cannot be excluded that U_{eff} may depend on the defect concentration due to the screening processes induced by delocalized charge carriers. The effect of U_{eff} as well as the vacancy concentration on the band gap in $Fe_{1-x}O$ are displayed in Fig. 4. We observe that the energy gap of each $Fe_{1-x}O$ composition decreases linearly upon decreasing U_{eff}. Particular declines in the band-gap energies are characterized by different slopes, i.e., the lower the x, the higher the slope. Obviously, the structures with higher vacancy concentrations exhibit more reduced energy gaps compared to that of defect-free FeO, mainly due to the increased number of empty Fe^{3+} states induced in the gap. These states are located just below the conduction band dominated by the unoccupied electronic states arising from the Fe^{2+} ions that hybridize with the unoccupied states of oxygen anions (see Fig. 2). The best agreement with the experimental energy gap of 1.15 eV, measured for $Fe_{1-x}O$ with $x = 7\%$ at 4.2 K [22], is found for $U_{\text{eff}} = 4$ eV. The unoccupied trivalent states constitute a band having the width increasing nonlinearly with increasing vacancy concentration, as shown for typical $U_{\text{eff}} = 5$ eV in the inset of Fig. 4. Similar behavior is also observed for the remaining values of U_{eff}, although the lower values of the Hubbard interaction result in more pronounced broadening of that band. Application of $U_{\text{eff}} = 2$ eV leads each $Fe_{1-x}O$ composition to a metallic state and to the disappearance of trivalent states in the wüstite lattice. In this case, all Fe cations become divalent with the average value of the spin magnetic moment of 3.57 μ_B.

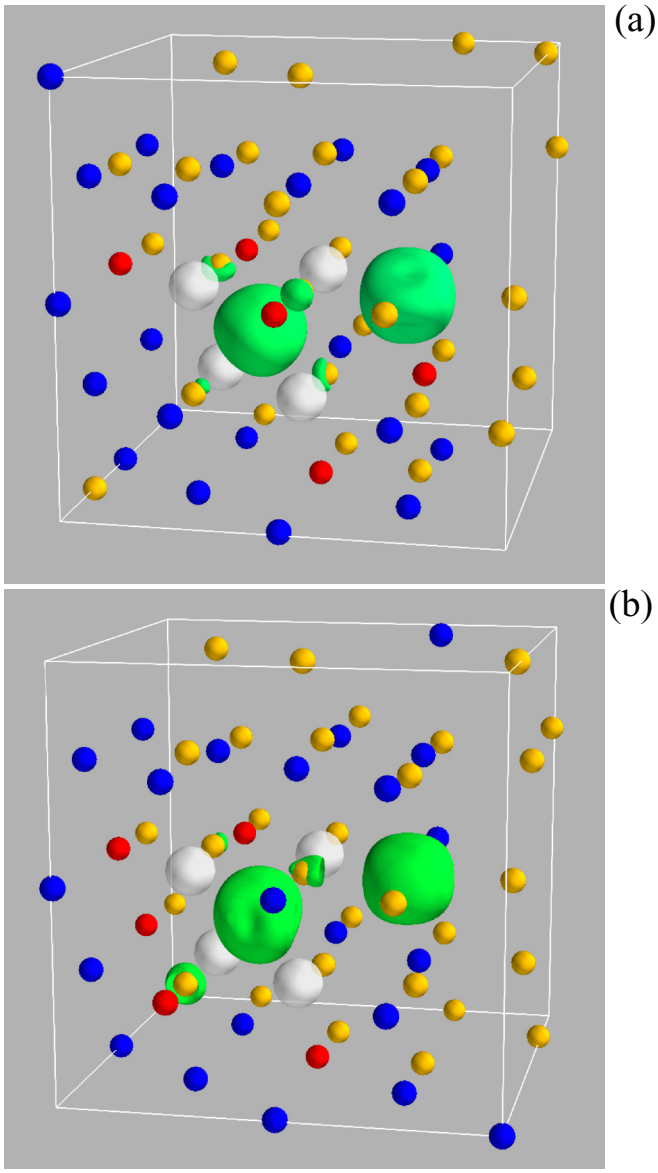

FIG. 3. (Color online) Magnetization isosurfaces of Fe^{2+} and Fe^{2+} cations in $Fe_{1-x}O$ containing 4:1-type vacancy clusters ($x = 9\%$) calculated at $U_{\text{eff}} = 5$ eV. (a) Configuration with the Fe^{2+} ion at the R site and the Fe^{3+} ion at the I site, (b) configuration with the Fe^{2+} ion at the I site and the Fe^{3+} ion at the R site. The cation vacancies and the R sites of Fe^{3+} ions are denoted, respectively, by white and red spheres, whereas the magnetization isosurface is marked in green. For clarity, the isosurfaces are drawn only for the I site and one selected R site. Note the relatively random distribution of Fe^{3+} ions around the 4:1 defect.

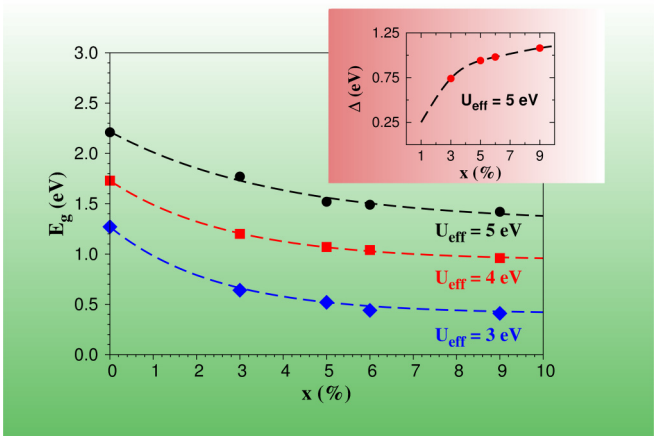

FIG. 4. (Color online) Influence of local interaction U_{eff} and vacancy concentration x on the energy gap E_g in $Fe_{1-x}O$. The inset shows the bandwidth (Δ) of the empty states of Fe^{3+} cations as a function of increasing x for $U_{\text{eff}} = 5$ eV. Dashed lines are guides for the eye.

IV. OPTICAL PROPERTIES

A. Dielectric functions

In general, the frequency-dependent dielectric function of a solid is a complex tensor,

$$\varepsilon(\omega) = \varepsilon_1(\omega) + i\varepsilon_2(\omega). \quad (2)$$

It can be used to characterize the linear response of a system to electromagnetic radiation. The real $\varepsilon_1(\omega)$ and imaginary $\varepsilon_2(\omega)$ parts of $\varepsilon(\omega)$ describe dispersion and absorption of the radiation in a given material, respectively. In addition, the zero-frequency limit of $\varepsilon_1(\omega)$ corresponds to the electronic part of the static dielectric constant of a material ϵ_∞, a parameter being of fundamental importance in many aspects of material properties, whereas $\varepsilon_2(\omega)$ is more specific and remains closely related to the band structure of the system.

The calculated dielectric function Eq. (2) of wüstite may exhibit anisotropic behavior due to the rhombohedral distortion induced by the AFII ordering and the removal of symmetry constraints arising from the presence of defects. Indeed, the results of our calculations indicate subtle differences among the components of $\varepsilon(\omega)$ along the main crystallographic directions in the considered vacancy-defected systems of FeO. Nevertheless, one can neglect this effect as too tiny to be observed experimentally and consider the averaged values of $\varepsilon_1(\omega)$ and $\varepsilon_2(\omega)$.

Figure 5 shows that both components of $\varepsilon(\omega)$ remain sensitive to the vacancy concentration in the regime of low photon energies (<8 eV), while at higher energies the differences between dielectric functions in the systems with different x are insignificant. Although ϵ_∞ increases with increased x, the shift upward does not exceed 10% within the studied range of vacancy concentrations. The calculated values of ϵ_∞ at $U_{\text{eff}} = 5$ eV vary from 5.24 to 5.53—they correspond closely to the experimental $\epsilon_\infty = 5.38$ given by Hofmeister *et al.* [19] and the theoretical value determined for perfectly stoichiometric FeO. On the other hand, one notes a broad range of ϵ_∞ values deduced from a variety of experiments [17,18,21–23], which extends from 9.6 to 13.

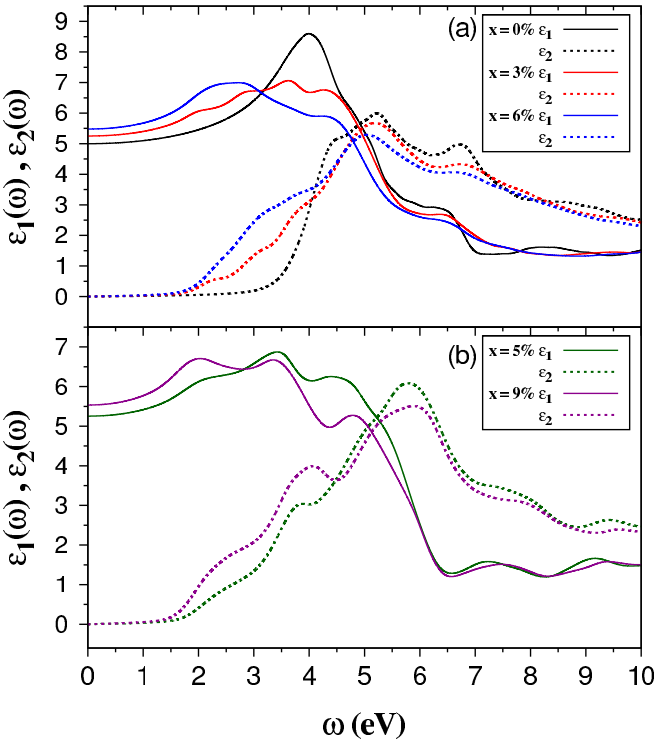

FIG. 5. (Color online) Real and imaginary parts of dielectric function (2) vs photon energy for (a) FeO with isolated vacancies and (b) FeO with vacancy clusters. Calculations are performed with $U_{\text{eff}} = 5$ eV.

A considerably larger value of ϵ_∞ in $Fe_{1-x}O$ in comparison to typical $\epsilon_\infty \approx 5$ for the remaining simple transition-metal oxides (MnO, CoO, NiO) used to be ascribed to a large Fe deficiency reaching up to several percent [17]. Much higher values of ϵ_∞ derived from experimental spectra may indicate the existence of a large amount of delocalized charge carries in the highly nonstoichiometric samples that can be easily polarized enhancing the value of ϵ_∞. One should also be aware that the static dielectric constant is measured at finite temperature and involves a contribution arising from phonons, whereas the majority of the calculations are actually performed for a static crystal (zero temperature and neglecting zero-point vibrations) and hence they report values due to the purely electronic screening. This can be an additional source of errors, unless the phonon contribution is carefully extracted from the spectra.

The $\varepsilon_2(\omega)$ spectra clearly show the redshift of the absorption edge and reduction of the optical gap with increasing vacancy concentration. The decrease of the optical gap from ~2.2 to ~1.5 eV while going from defect-free FeO to $Fe_{1-x}O$ results from the presence of the Fe^{3+} states in the band gap. A substantial reduction of the band gap in $Fe_{1-x}O$ with vacancy content ranging from 7% to 8% has been revealed by the recent infrared reflectivity and ellipsometry experiments [22,24]. These studies provide a value of the fundamental absorption edge in wüstite of 1.15 eV at 5 K and 1.0–1.3 eV at room temperature.

The absorption spectra of $Fe_{1-x}O$ with different concentrations of vacancies show many common features. First of all, the spectra are dominated by a wide and intense peak

at 5.2 eV, which shifts slightly to lower (higher) energies for $Fe_{1-x}O$ systems containing isolated vacancies (vacancy clusters). Another similarity is connected with the broad and less intense peak at 6.7 eV moving upward by about 1 eV but only in wüstite containing vacancy clusters. Generally, both peaks diminish their intensities with the increased defect content. The absorption spectra exhibit broad distribution in the energy range of 10–25 eV and a structureless plateau declining progressively at still higher photon energies.

There are, however, prominent differences in $\varepsilon_2(\omega)$ spectra between systems with isolated vacancies and 4:1-type clusters. They are encountered mainly below 4.5 eV and reflect differences in the electronic structures between those systems (cf. Fig. 2 and Fig. 1 in Ref. [14]). In the absorption spectra of wüstite containing isolated vacancies, the shoulder extending from about 1.5 to 4 eV originates from interband transitions that involve states of Fe^{3+} and Fe^{2+} ions residing in R lattice positions as well as the oxygen states that are always hybridized with cation states. The respective feature in wüstite with vacancy clusters gets a better resolved structure with a peak emerging at 4 eV and a tail with small swelling centered just above 2 eV. The 4 eV peak originates solely from the transitions due to the states of Fe^{2+} ions at the R or I sites, provided the latter are present in the lattice [cf. the densities of electronic states in Figs. 2(a) and 2(b)].

On the other hand, the Fe^{3+} states, either from R or I sites, that have the most considerable contribution inside the band gap, give rise to transitions observed at an energy in the vicinity of 2 eV. It is worth noting that the swelling at 2 eV immerses into the broad distribution when Fe^{3+} ions occupy only the R sites. In such a case, the low-energy $\varepsilon_2(\omega)$ spectrum of wüstite with 4:1-type clusters resembles the $\varepsilon_2(\omega)$ spectrum of wüstite with isolated vacancies. Therefore, the swelling can be assigned to transitions involving trivalent Fe cations at interstitial lattice positions. Moreover, an exact identification of the transitions that are responsible for the peaks in the $\varepsilon_2(\omega)$ spectra of $Fe_{1-x}O$ is hindered by a strong overlap and hybridization of the s, p, and d states in both the valence and conduction bands. This effect has already been pointed out for perfectly stoichiometric FeO by Rödl *et al.* [13].

B. Comparison with experiments

Optical-absorption spectra extracted from the reflectivity measurements [20] on wüstite with nonstoichiometry of the order of several percent show a very broad peak at about 4.5 eV and strongly enhanced absorption at low photon energies (see Fig. 6). The latter is absent in our calculated $\varepsilon_2(\omega)$ spectra obtained for $U_{\text{eff}} = 3$–5 eV. Some discrepancy between our theoretical results for $\varepsilon_2(\omega)$ and those derived from the experiment [20] remains unclear, especially the fact that both $\varepsilon_1(\omega)$ functions agree reasonably well in the line shape and magnitude within the energy range of 1–5 eV. We note, however, that the theoretical and experimental results are inconsistent below ∼1 eV due to abrupt growth of the experimental spectral amplitude of $\varepsilon(\omega)$. Such peculiar behavior of both $\varepsilon_1(\omega)$ and $\varepsilon_2(\omega)$ (not encountered in MnO, CoO, and NiO) was also observed in the data obtained from the ellipsometry spectroscopy [24] and has been attributed to defect absorption at Fe vacancies. Indeed, the experimental $\varepsilon_1(\omega)$ and $\varepsilon_2(\omega)$ spectra exhibiting growth with $\omega \to 0$ seem to reflect the narrow-gap nature of $Fe_{1-x}O$ at vacancy concentrations of the order of several percent.

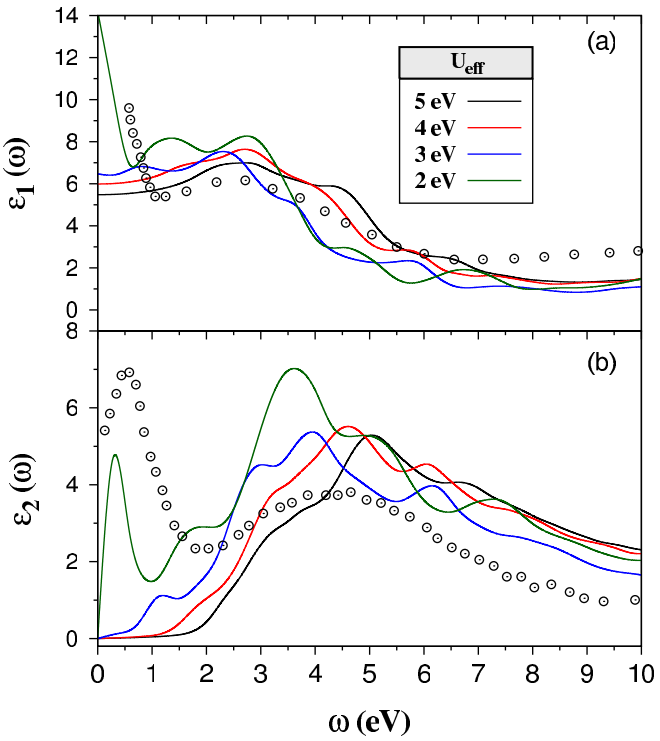

FIG. 6. (Color online) Dependence of (a) real and (b) imaginary parts of the dielectric function on U_{eff} for $Fe_{1-x}O$ with $x = 6\%$. The values derived from the experiment (open symbols) are adopted from Ref. [20].

The increase in absorption spectra at low energies, typical for metals (Drude peak), indicates the existence of delocalized charge carriers despite the Mott insulator state of wüstite. These itinerant carriers (electrons or holes) exist due to the defected structure of $Fe_{1-x}O$. Such a complicated electronic structure is difficult to model within the DFT approach. However, the effect of wüstite *metallization* can be simulated to some extent by lowering the Hubbard parameter U on the Fe cations.

The results of such investigations are depicted in Fig. 6. One observes shifting of the peak's positions to lower energies with decreasing U_{eff} from 5 to 4 eV. At still lower U_{eff}, the spectra acquire a more complex pattern composed of additional peaks appearing at low ω, and finally the $Fe_{1-x}O$ system transforms to a metallic state at $U_{\text{eff}} = 2$ eV. The $\varepsilon_2(\omega)$ spectrum shows a Drude-like peak at low energies, in good agreement with the data derived from the experiment. The *metallization* arising from its large off-stoichiometry also affects the real part of the dielectric function, which displays pronounced growth at low ω, which in turn yields a substantial increase of the electronic part of the static dielectric constant ($\epsilon_\infty = 14.2$). This phenomenon is likely to be responsible for the characteristic features of wüstite dielectric functions detected in a variety of experiments and commonly interpreted as defect-related effects.

The real and imaginary components of $\varepsilon(\omega)$ are usually determined from ellipsometry experiments or derived from

absorption, reflection, or transmission measurements after the Kramers-Kronig analysis. The experimental data are frequently presented in the form of the reflectivity spectrum [42],

$$R(\omega) = \left| \frac{\sqrt{\varepsilon(\omega)} - 1)}{\sqrt{\varepsilon(\omega)} + 1)} \right|^2 = \frac{[n(\omega) - 1]^2 + k^2(\omega)}{[n(\omega) + 1]^2 + k^2(\omega)}, \quad (3)$$

where

$$n(\omega) = \sqrt{\frac{|\varepsilon(\omega)| + \varepsilon_1(\omega)}{2}}, \quad (4)$$

$$k(\omega) = \sqrt{\frac{|\varepsilon(\omega)| - \varepsilon_1(\omega)}{2}}. \quad (5)$$

The functions $n(\omega)$ and $k(\omega)$ denote, respectively, the refractive index and extinction coefficients that constitute the complex refractive index,

$$N(\omega) = \sqrt{\varepsilon(\omega)} = n(\omega) + ik(\omega). \quad (6)$$

A comparison between the results of calculations performed as a function of x and the recent ellipsometry experiments carried out on samples with $x = 7.5\%$ [24] is given in Fig. 7. Similarly to the dielectric functions, the calculated spectra shift to lower energies for a larger concentration of defects. Thus, the zero-energy limit of the reflectivity and the refractive index increases and the absorption edge visible in the extinction coefficient diminishes with the increasing x. Despite small differences, one finds that the calculated $R(\omega)$, $n(\omega)$, and $k(\omega)$ spectra reflect reasonably well the behavior of the respective experimental quantities above ∼1.5 eV. Both experimental and calculated data indicate an increase in the reflectivity of $Fe_{1-x}O$ by almost 10% between 1.5 and 5.0 eV, and the reflectivity decreases above this energy range. A visible mismatch between theoretical and experimental results is observed at low photon energies, where the measured quantities show a pronounced increase, probably due to the higher amount of free charge carriers embedded in the measured samples as well as much stronger absorption by defects in comparison with the simulated $Fe_{1-x}O$ systems.

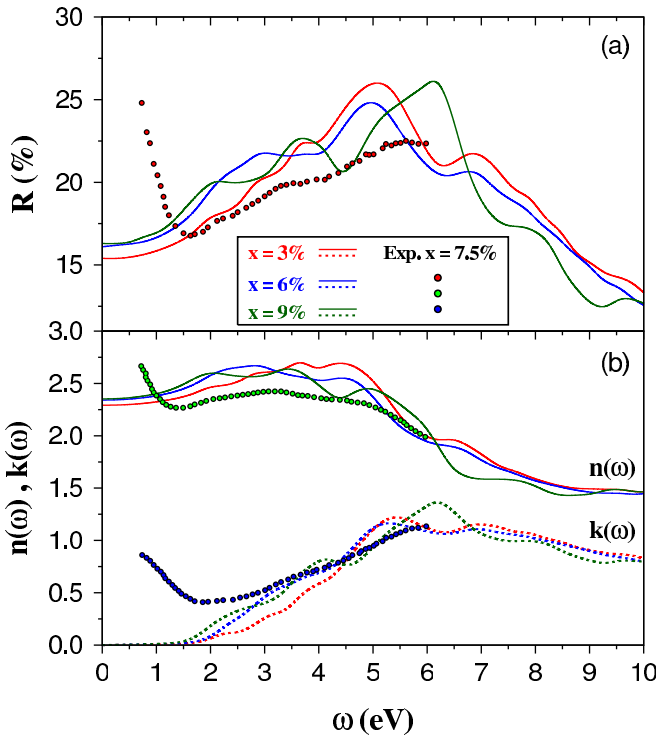

FIG. 7. (Color online) (a) Reflectivity $R(\omega)$, (b) refractive index $n(\omega)$ and extinction coefficient $k(\omega)$ of $Fe_{1-x}O$ with different nonstoichiometry. Theoretical and experimental data [24] are denoted by solid and dashed lines and symbols, respectively. Theoretical results are obtained for $U_{\text{eff}} = 5$ eV.

A deficiency in the wüstite cation sublattice was also suggested to be responsible for the large spectral linewidth of the transverse-optic (TO) phonon obtained from the infrared reflectivity measurements [22,23]. One finds that the dielectric loss spectrum of the paramagnetic $Fe_{1-x}O$ contains a broad and symmetric single line peaked at about 325 cm^{-1}, whereas the antiferromagnetic $Fe_{1-x}O$ reveals a weakly resolved two-peak structure, making the low-temperature experimental spectrum asymmetric. This feature is also observed in our Gaussian convoluted infrared absorption spectrum, which is directly related to the dielectric loss function. Indeed, as depicted in Fig. 8, both theoretical and experimental infrared absorption spectra show much broader distributions of the TO phonon frequencies than those in more stoichiometric simple $3d$ transition-metal oxides (MnO, CoO, and NiO) [23].

The broad theoretical spectrum arises from the splitting of phonon frequencies due to the crystal symmetry being lowered by the presence of defects. The δ functions, shown in Fig. 8, represent the infrared intensity δ peaks associated with the splitted frequencies, subsequently convoluted with the experimental Gaussian width. It appears that the maximum of the convoluted spectral peak for the simulated compositions of $x = 5\%$ and 6% shifts to higher frequencies (330 and 342 cm^{-1}) in comparison with the position of the respective peak in the defect-free FeO (324 cm^{-1}). Also, the main peak in

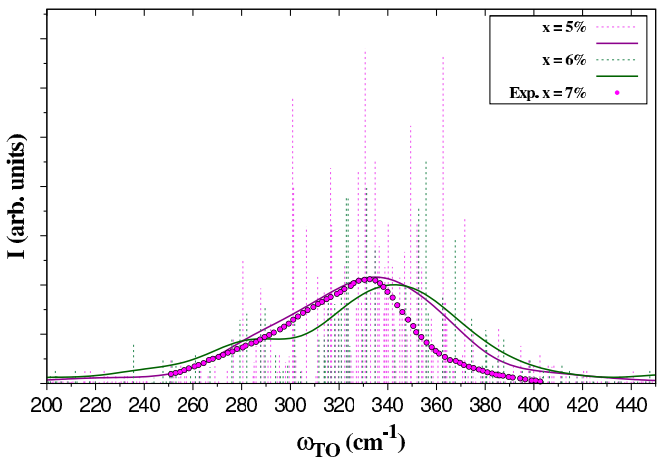

FIG. 8. (Color online) Theoretical infrared absorption intensities (dotted vertical lines) of $Fe_{1-x}O$ with the Fe-vacancy content of 5% (vacancy clusters) and 6% (isolated vacancies) and the Gaussian convolutions of theoretical spectra with a FWHM of 33 cm^{-1} (solid lines). The experimental dielectric loss function [22] measured at 5 K for $Fe_{1-x}O$ with $x = 7$–8 % is represented by solid symbols. The frequencies ω_{TO} correspond to the transverse-optic phonons. Theoretical results are obtained for $U_{\text{eff}} = 5$ eV.

the Gaussian convoluted infrared absorption spectra changes its position from 338 to 319 cm^{-1}, while increasing x from 3% to 9% (not shown).

A similar trend to the one observed here has already been encountered in the early infrared reflectivity experiments [16] performed on wüstite samples with different concentrations of cation vacancies. Such a strong sensitivity of the infrared spectra to the concentration of defects can account for a large scattering seen in the experimentally determined TO phonon frequencies in wüstite, which cover the range extending from 320 to 410 cm^{-1} [18,19,21–23]. The broadening and shifting of the infrared spectral peaks seem to have the same origin as very similar changes observed in the phonon density of states [14], and they reflect pronounced modifications of the electronic structure and force constants due to cation vacancies in the Fe sublattice of wüstite.

V. SUMMARY AND CONCLUSIONS

This work investigates the role of strong electron correlations on Fe atoms and the high concentration of cation vacancies in modifying the electronic and dielectric properties of wüstite ($Fe_{1-x}O$). As we have shown, both of them influence substantially the electronic properties of this compound and have the opposite effect on its band structure. While the local electron interactions in the Fe $3d$ states are responsible for the opening of the insulating gap, the Fe vacancies reduce its magnitude. The mechanism of gap reduction remains the same, irrespective of the type of incorporated defects. Either monovacancies or vacancy clusters induce the band of empty Fe^{3+} states inside the gap of the perfect FeO crystal. The width of this band increases monotonically with the increased concentration of cation vacancies reducing the distance from the top of the valence states, thus effectively diminishing the band gap.

The strength of the effective local interaction U_{eff} depends presumably on the vacancy content, i.e., the band-gap reduction enhances the screening of Coulomb interactions, which may lead to even larger electron mobility and *metallization* of iron oxide. The presence of free charge carriers, modeled here by small values of U_{eff}, explains the increase of the dielectric function and optical reflectivity observed experimentally at low energies.

Summarizing, we presented several effects observed in the optical properties of wüstite, and we explained them by the presence of defects. We emphasize that our studies also explain the anomalous broadening of infrared spectra, demonstrating a strong effect of cation vacancies on phonons in wüstite. Similar correlations between charge distribution and lattice dynamics induced by the electron-phonon coupling play an important role in the Verwey transition in magnetite (Fe_3O_4) [43]. As noticed recently [15], also the polaronic distribution found in defected FeO resembles the charge-orbital order in magnetite and may share a common origin with the short-range order observed above the Verwey temperature [44]. Finally, we point out that the effects discussed here are relevant not only for iron oxides, but they are expected to determine the electronic, dielectric, and dynamical properties of other strongly correlated systems with high concentrations of intrinsic defects as well.

ACKNOWLEDGMENTS

The authors acknowledge valuable discussions with Małgorzata Sternik and Jan Łażewski, Institute of Nuclear Physics, Polish Academy of Sciences, Cracow, Poland. The Interdisciplinary Center for Mathematical and Computational Modeling (ICM), Warsaw University, Poland and the IT4Innovations National Supercomputing Center, VSB-Technical University, Ostrava, Czech Republic are acknowledged for providing the computer facilities under Grants No. G28-12 and Reg. No. CZ.1.05/1.1.00/02.0070. The authors acknowledge support by Narodowe Centrum Nauki (NCN, National Science Center) under Projects No. 2011/01/M/ST3/00738 and No. 2012/04/A/ST3/00331.

[1] W. L. Roth, Acta Crystallogr. **13**, 40 (1960); D. S. Tannhauser, J. Phys. Chem. Solids **23**, 25 (1962); F. Koch and J. B. Cohen, Acta Crystallogr. Sect. B **25**, 275 (1969); A. K. Cheetham, B. E. F. Fender, and R. I. Taylor, J. Phys. C **4**, 216 (1971).

[2] B. Andersson and J. O. Sletnes, Acta Crystollogr. **33**, 268 (1977); E. Bauer and A. Pianelli, Mat. Res. Bull. **15**, 177 (1980); A. Yamamoto, Acta Crystallogr. B **38**, 1451 (1982).

[3] C. A. McCammon and L.-G. Liu, Phys. Chem. Miner. **10**, 106 (1984).

[4] C. A. McCammon and D. C. Price, Phys. Chem. Miner. **11**, 250 (1985).

[5] C. A. McCammon and Q. A. Pankhurst, Hyperfine Interact. **94**, 1989 (1994).

[6] R. M. Hazen and R. Jeanloz, Rev. Geophys. Space Phys. **22**, 37 (1984).

[7] G. J. Long and F. Grandjean, in *Advances in Solid State Chemistry*, edited by C. R. A. Catlow (JAI, London, 1991), Vol. 2, p. 187.

[8] C. R. A. Catlow and B. E. F. Fender, J. Phys. C **8**, 3267 (1975).

[9] M. R. Press and D. E. Ellis, Phys. Rev. B **35**, 4438 (1987).

[10] P. K. Khowash and D. E. Ellis, Phys. Rev. B **39**, 1908 (1989).

[11] W. Schweika, A. Hoser, M. Martin, and A. E. Carlsson, Phys. Rev. B **51**, 15771 (1995).

[12] F. Tran, P. Blaha, K. Schwarz, and P. Novák, Phys. Rev. B **74**, 155108 (2006); C. Rödl, F. Fuchs, J. Furthmüller, and F. Bechstedt, **79**, 235114 (2009); H. Jiang, R. I. Gomez-Abal, P. Rinke, and M. Scheffler, **82**, 045108 (2010).

[13] C. Rödl and F. Bechstedt, Phys. Rev. B **86**, 235122 (2012).

[14] U. D. Wdowik, P. Piekarz, K. Parlinski, A. M. Oleś, and J. Korecki, Phys. Rev. B **87**, 121106(R) (2013).

[15] I. Bernal-Villamil and S. Gallego, Phys. Rev. B **90**, 195126 (2014).

[16] K. Bowen, D. Adler, and B. H. Auker, J. Solid State Chem. **12**, 355 (1975).

[17] B. Prévot, J. Biellmann, M. F. Meftah, and M. Sieskind, Phys. Status Solidi A **40**, 503 (1977).

[18] G. Kugel, C. Carabatos, B. Hennion, B. Prevot, A. Revcolevschi, and D. Tocchetti, Phys. Rev. B **16**, 378 (1977).
[19] A. M. Hofmeister, E. Keppel, and A. K. Speck, Mon. Not. R. Astron. Soc. **345**, 16 (2003).
[20] N. Hiraoka, H. Okamura, H. Ishii, I. Jarrige, K. D. Tsuei, and Y. Q. Cai, Eur. Phys. J. B **70**, 157 (2009).
[21] C. T. Seagle, W. Zhang, D. L. Heinz, and Z. Liu, Phys. Rev. B **79**, 014104 (2009).
[22] F. Schrettle, C. Kant, P. Lunkenheimer, F. Mayr, J. Deisenhofer, and A. Loidl, Eur. Phys. J. B **85**, 164 (2012).
[23] C. Kant, M. Schmidt, Z. Wang, F. Mayr, V. Tsurkan, J. Deisenhofer, and A. Loidl, Phys. Rev. Lett. **108**, 177203 (2012).
[24] J.-W. Park, S. Kim, S.-H. Choi, and H. Lee, New Phys.: Sae Mulli **63**, 818 (2013).
[25] G. Kresse and J. Furthmüller, Phys. Rev. B **54**, 11169 (1996); Comput. Mater. Sci. **6**, 15 (1996).
[26] P. E. Blöchl, Phys. Rev. B **50**, 17953 (1994); G. Kresse and D. Joubert, *ibid.* **59**, 1758 (1999).
[27] J. P. Perdew, J. A. Chevary, S. H. Vosko, K. A. Jackson, M. R. Pederson, D. J. Singh, and C. Fiolhais, Phys. Rev. B **46**, 6671 (1992).
[28] S. L. Dudarev, G. A. Botton, S. Y. Savrasov, C. J. Humphreys, and A. P. Sutton, Phys. Rev. B **57**, 1505 (1998).
[29] U. D. Wdowik and K. Parlinski, Phys. Rev. B **78**, 224114 (2008); J. Phys.: Condens. Matter **21**, 125601 (2009).
[30] U. D. Wdowik, Phys. Rev. B **84**, 064111 (2011).
[31] W. L. Roth, Phys. Rev. **110**, 1333 (1958).
[32] M. Gajdoš, K. Hummer, G. Kresse, J. Furthmüller, and F. Bechstedt, Phys. Rev. B **73**, 045112 (2006).
[33] P. Blaha, K. Schwarz, G. K. H. Madsen, D. Kvasnicka, and J. Luitz, *Wien2k, An Augmented Plane Wave and Local Orbitals Program for Calculating Crystal Properties*, edited by K. Schwarz (Vienna University of Technology, Austria, 2012).
[34] V. I. Anisimov, I. V. Solovyev, M. A. Korotin, M. T. Czyżyk, and G. A. Sawatzky, Phys. Rev. B **48**, 16929 (1993).
[35] *Mössbauer Isomer Shifts*, edited by G. K. Shenoy and F. E. Wagner (North-Holland, Amsterdam, 1978).
[36] U. D. Wdowik and K. Ruebenbauer, Phys. Rev. B **76**, 155118 (2007).
[37] R. Vidya, P. Ravindran, H. Fjellvag, B. G. Svensson, E. Monakhov, M. Ganchenkova, and R. M. Nieminen, Phys. Rev. B **83**, 045206 (2011); C. Freysoldt, B. Grabowski, T. Hickel, J. Neugebauer, G. Kresse, A. Janotti, and C. G. Van de Walle, Rev. Mod. Phys. **86**, 253 (2014).
[38] R. M. Cornell and U. Schwertmann, *The Iron Oxides, Structure, Properties, Reactions, Occurence and Uses* (Wiley-VCH, Weinheim, 2003); S. Krehula, G. Štefanić, K. Zadro, L. K. Krehula, M. Marciuš, and S. Musić, J. Alloys Compd. **545**, 200 (2012).
[39] R. S. Hargrove and W. Kündig, Solid State Commun. **8**, 303 (1970); F. J. Berry, S. Skinner, and M. F. Thomas, J. Phys.: Condens. Matter **10**, 215 (1998); I. Dézsi, C. Fetzer, Á. Gombkötö, I. Szücs, J. Gubicza, and T. Ungár, J. Appl. Phys. **103**, 104312 (2008).
[40] G. K. Wertheim, Phys. Rev. **124**, 764 (1961); K. Ruebenbauer and U. D. Wdowik, J. Phys. Chem. Solids **65**, 1785 (2004).
[41] D. P. Johnson, Solid State Commun. **7**, 1785 (1969); L. F. Checherskaya, V. P. Romanov, and P. A. Tatsienko, Phys. Status Solidi A **19**, K177 (1973).
[42] M. Fox, *Optical Properties of Solids* (Oxford University Press, New York, 2001).
[43] P. Piekarz, K. Parlinski, and A. M. Oleś, Phys. Rev. Lett **97**, 156402 (2006); Phys. Rev. B **76**, 165124 (2007); M. Hoesch, P. Piekarz, A. Bosak, M. Le Tacon, M. Krisch, A. Kozłowski, A. M. Oleś, and K. Parlinski, Phys. Rev. Lett. **110**, 207204 (2013).
[44] A. Bosak, D. Chernyshov, M. Hoesch, P. Piekarz, M. Le Tacon, M. Krisch, A. Kozłowski, A. M. Oleś, and K. Parlinski, Phys. Rev. X **4**, 011040 (2014).